Research Square

Preprints are preliminary reports that have not undergone peer review.
They should not be considered conclusive, used to inform clinical practice,
or referenced by the media as validated information.

Electron Shuttle Waiting Times for Electric Field Sensing

Alberto Mayorgas

alberto.mayorgasreyes@ceu.es

Universidad CEU Fernando III

Alberto López-García

Universidad Politécnica de Cartagena

Enamul Haque

Universidad Politécnica de Cartagena

Javier Cerrillo

Universidad Politécnica de Cartagena

Research Article

Keywords:

Posted Date: November 6th, 2026

DOI: https://doi.org/10.21203/rs.3.rs-11394533/v1

License: This work is licensed under a Creative Commons Attribution 4.0 International License.
Read Full License

Additional Declarations: No competing interests reported.

Electron Shuttle Waiting Times for Electric Field Sensing

Alberto Mayorgas [1,*] Alberto López-García [2] Enamul Haque [2] and Javier Cerrillo [2,†]

[1] *Universidad CEU Fernando III, CEU Universities, Escuela Politécnica Superior, Glorieta Cardenal Herrera Oria, 41930 Seville, Spain*

[2] *Universidad Politécnica de Cartagena member of European Uniersity of Technology EUT+, Research Group of Quantum Technologies, Área de Física Aplicada, Cartagena E-30202, Spain*

(Dated: October 16, 2026)

ABSTRACT

We explore the use of waiting time statistics in a quantum electron shuttle for electric-field sensing. Electron shuttles convert nanomechanical motion into charge transport, showing a noise-broadened crossover between stochastic tunneling and mechanically assisted charge transfer. This allows investigation of how transport fluctuations encode electromechanical parameters. Using a single-level quantum shuttle in strong-Coulomb-blockade and high-bias regimes with a Markovian quantum master equation, we analyze stationary dynamics in phase space and waiting time distributions. By estimating the electromechanical coupling, proportional to the electric field, we evaluate the classical Fisher information in waiting times and compare it with the quantum Fisher information in the stationary state. We relate the metrological response to mean waiting time, variance, and Fano factor. Our results show that the crossover from tunneling to shuttling is characterized by enhanced fluctuations and increased parameter sensitivity, leading to a pronounced enhancement of the Fisher information.

I. INTRODUCTION

Nanoelectromechanical systems (NEMS) provide a natural platform for studying the interplay between charge transport and mechanical motion. In these systems, charge-carrier tunneling exerts a force on a movable mechanical element, whose displacement in turn modulates the tunneling amplitudes. A paradigmatic example is the electron shuttle, in which a small island or quantum dot oscillates between two leads and transfers charge carriers through repeated loading and unloading events. The theoretical concept of the NEMS electron shuttle was introduced in [1] and subsequently realized experimentally in flexible nanoresonators, carbon-based molecular systems, and metal nanoparticle structures [2–4].

The shuttle mechanism describes a self-sustained charge-transfer process in which mechanical motion cooperates with sequential tunneling [1, 5, 6]. Depending on the electromechanical coupling, the system can operate in distinct transport regimes. In the tunneling regime, charge transfer is dominated by stochastic tunneling and the mechanical oscillator remains localized near equilibrium. In the shuttling regime, charge transfer becomes synchronized with the mechanical motion. Between them lies a crossover region where stochastic tunneling and mechanically assisted transport coexist [7, 8]. While the classical description predicts a relatively sharp transition between these regimes, quantum fluctuations smooth this instability into a crossover [9–13]. The resulting stationary quantum state can be characterized in phase space through quasi-probability distributions such as the Wigner or Husimi functions [7].

The dependence of transport on the electromechanical coupling is commonly characterized through current fluctuations and, more recently, through waiting time distributions (WTDs), which describe the temporal correlations between successive tunneling events [14–24]. In contrast to stationary current and low-order cumulants, WTDs directly probe the temporal structure of individual charge-transfer events and can reveal the emergence of electron emission synchronized with the mechanical motion. Their ability to distinguish tunneling and shuttling dynamics has been demonstrated in both classical [25] and quantum [26] shuttle models.

The same transport record can also be viewed through the lens of quantum metrology. Transport measurements encode information about parameters that are not directly accessible, as these leave measurable signatures in the statistics of tunneling events [27–30]. A central question is therefore how much information about a given parameter can be extracted from the observed transport data. This is quantified by the classical Fisher information (CFI), which measures the sensitivity of the measured probability distribution to variations of the parameter [31–33]. At the level of the underlying quantum state, the quantum Fisher information (QFI) represents the maximum information that can be encoded about the same parameter and thus provides an upper bound on the CFI [34–36].

Enhanced values of both the CFI and QFI are often associated with critical phenomena, where small parameter variations can induce large changes in the state or

* alberto.mayorgasreyes@ceu.es

† javier.cerrillo@upct.es

dynamics of the system. This observation underlies the concept of quantum critical sensing, in which the strong susceptibility near a critical point is exploited to achieve enhanced parameter-estimation precision [37, 38]. While originally developed in the context of equilibrium quantum phase transitions, the idea has since been extended to finite-size and driven-dissipative systems, where bifurcations and dynamical transitions can likewise give rise to enhanced parameter sensitivity and Fisher information [39–43]. In monitored open quantum systems, these enhancements can be directly reflected in experimentally accessible measurement records through increased CFI [40]. This raises a natural question for the electron shuttle: can the crossover between tunneling and shuttling regimes, controlled by the electromechanical coupling, provide an enhanced metrological response, and to what extent is this enhancement accessible through experimentally measured tunneling statistics?

Here, we investigate this question for a quantum shuttle described by a Markovian master equation in the regimes of strong Coulomb blockade and high bias. We characterize the stationary island-oscillator state through its Husimi representation and identify the tunneling, crossover, and shuttling regimes. We then analyze the waiting time distribution between successive tunneling events and its first two moments and Fano factor. Treating the electromechanical coupling as the parameter to be estimated, we calculate the CFI associated with the complete waiting time distribution and compare it with the QFI in the stationary quantum state. We find that enhanced waiting-time noise and enhanced parameter sensitivity both emerge in the crossover region, although their maxima do not generally coincide. These results establish a connection between transport fluctuations and metrological sensitivity in the quantum shuttle and suggest the electromechanical crossover as a possible resource for electric field quantum sensing.

II. MODEL

Let us consider a quantum dot with a single electronic level oscillating between source and drain electrodes. The device can be viewed as a gate-free single-electron transistor (SET), in which the dot's motion modulates the tunneling rates to the leads, shuttling electrons from the source to the drain under an applied bias and thereby generating a net current. Throughout this work, we consider the strong Coulomb-blockade regime, which restricts the island occupancy to at most a single excess electron. The Hamiltonian of the full system can be decomposed in four terms

$$H_{\mathrm{T}} = H_{\mathrm{S}} + H_{\mathrm{L}} + H_{\mathrm{tun}} + H_{\mathrm{B}}. \tag{1}$$

The first term is the island-oscillator Hamiltonian H_{S}. The electronic single state on the dot is described by the fermionic operators $c, c^\dagger$, and the vibrational degree of

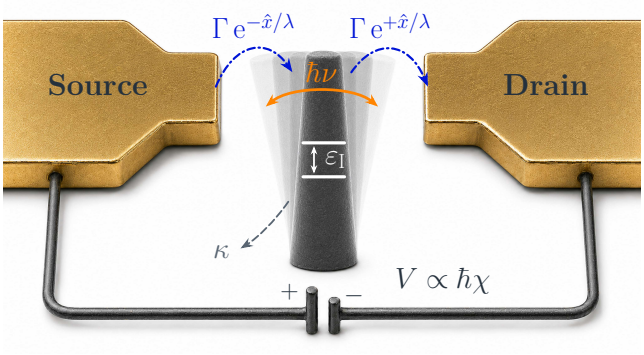


FIG. 1: Schematic representation of the electron shuttle. The central island (quantum dot) is modeled as a two-level system with energy spacing ε_{I}, indicated in white, and moves in a harmonic potential with energy quantum $\hbar\nu$, represented by the orange double-headed arrow. The blue dash-dotted arrows indicate position-dependent electron tunneling from the source to the island and from the island to the drain, with rates $\Gamma e^{-\hat{x}/\lambda}$ and $\Gamma e^{+\hat{x}/\lambda}$, respectively, where $\hat{x}$ is the island displacement and λ is the tunneling length. The applied bias V controls the island–oscillator coupling strength χ, while the gray dashed arrow denotes mechanical damping at rate κ due to coupling of the oscillator to a thermal bath.

freedom by the bosonic operators $a, a^\dagger$, with their respective anticommutation and commutation relations. The first Hamiltonian reads

$$H_{\mathrm{S}} = \varepsilon_{\mathrm{I}} c^\dagger c + \hbar\nu a^\dagger a - \hbar\chi c^\dagger c(a^\dagger + a)\,, \tag{2}$$

describing a two-level system (single electronic level) of energy ε_{I}, a quantum harmonic oscillator of frequency ν and a coupling term with strength χ proportional to the electric field due to the bias voltage between the left and right leads, that is, the electric field seen by an electron on the dot.

We glance over the rest of the terms in the Hamiltonian, for a detailed discussion see the references [44, 45] and Appendix A. The second component H_{L} characterizes the leads, the electrostatic energy of an ensemble of non-interacting electrons, which are in local equilibrium and described by the Fermi distribution. The third term H_{tun} is the tunnel coupling between the island and the leads. The tunneling amplitudes are proportional to the exponential $e^{\pm\hat{x}/\lambda}$, which is a function of the tunneling length λ and the distance of the island to the leads $\hat{x} = x_0(a + a^\dagger)$, where $x_0 = \sqrt{\hbar/2m\nu}$ is the zero point motion of the oscillator and m its mass. The fourth term H_{B} includes the coupling of the oscillator to a dissipative Ohmic heat bath in the rotating wave approximation (weak bilinear interaction) [46–48]. This produces damping and thermal noise in the mechanical system, and sets a boundary in the motion.

The master equation (ME) is derived by tracing the degrees of freedom of the leads and the heat bath, hence

the equation contains only the island-oscillator subsystem [10, 44],

$$\frac{d}{dt}\rho = -i\nu\left[a^\dagger a,\rho\right] + i\chi\left[c^\dagger c(a^\dagger + a),\rho\right] + \kappa\,\mathcal{D}\left[a\right]\rho \quad (3)$$
$$+ \Gamma\,\mathcal{D}\left[c\,e^{x_0(a^\dagger+a)/\lambda}\right]\rho + \Gamma\,\mathcal{D}\left[c^\dagger e^{-x_0(a^\dagger+a)/\lambda}\right]\rho,$$

where Γ is the rate of electron tunneling (equal for source-island and island-drain), κ the damping rate, and the dissipator is defined as [48]

$$\mathcal{D}\left[A\right]\rho = A\rho A^\dagger - \frac{1}{2}\{A^\dagger A,\rho\}, \quad (4)$$

with the $\{A,B\} = AB + BA$ the anticommutator. The density matrix has a size $2N \times 2N$ due to the tensor product Hilbert space of the island-oscillator, where N is the truncated size of the oscillator basis.

The master equation (3) is calculated in the Born-Markov approximation, that is the mechanical damping caused by the heat bath is addressed within the standard weak coupling theory and with a short bath correlation time [44, 48, 49]. Both estimations are combined with the rotating wave approximation to produce a quantum optical ME for the damping term. See [45] for a non-Markovian version of the ME. The bath is assumed to be in thermal equilibrium, with its occupation determined by the Bose-Einstein distribution. In the zero-temperature limit considered here [19], the thermal occupation vanishes, and the term $\mathcal{D}\left[a^\dagger\right]\rho$ does not appear in the ME (3). See Appendix A for more details about the approximations considered.

It is known that three distinct regimes are distinguished for the electron shuttle [10, 25, 44]:

I) *Tunneling (SET)*: The correlation between the mechanical motion and the tunneling dynamics can be suppressed in two distinct regimes. The first corresponds to strong mechanical dissipation (κ), for which the WTD exhibits a broad envelope extending over times $t \gg 2\pi/\nu$, approximately described by a Gamma distribution and weakly modulated by quantum fluctuations. The second occurs when tunneling dominates the mechanical dynamics ($\Gamma \gg \nu$), leading to a sharply peaked WTD at $t \ll 2\pi/\nu$, characteristic of transport through a conventional single-electron transistor. In both cases, electron transport becomes only weakly correlated with the oscillator motion. In the following, we focus on the regime of strong mechanical dissipation.

II) *Shuttle*: The tunneling rate is similar to the oscillator frequency $\Gamma \simeq \nu$, so the WTD profile is a single peak at $t = 2\pi/\nu$.

III) *Crossover*: Intermediate regime between SET and shuttle, where the WTD envelope shape changes from Gamma-like to exponential-like, and finally to a single peak (shuttle).

In our proposal, the coupling strength χ is treated as a tunable parameter that drives the system across different dynamical regimes. Since χ is proportional to the electric field generated by the applied bias voltage, varying χ is equivalent to tuning the voltage across the device. This makes the electric field the natural parameter to be estimated and provides a simple experimental control knob compared to quantities such as the tunneling rate Γ or the mechanical damping κ.

III. RESULTS

A. Stationary state and waiting time distribution

The stationary solution of the master equation (3) is calculated using the vectorization procedure, which transforms the Lindblad form of the master equation $\mathcal{L}\rho_0 = 0$ into a system of linear equations $4N^2 \times 4N^2$. Appendix B provides more details of the vectorization process and the challenges of finding the solution ρ_0 of the system. Unless otherwise indicated, we use the set of parameters $\Gamma = 0.01\nu$, $\kappa = 0.05\nu$, $\lambda = 2x_0$ and an oscillator basis of size $N = 50$. The coupling $\chi \in [0.1, 0.6]$ varies in a 100 element interval. For these parameters, the convergence of the stationary solution calculation is ensured since the residual remains low: $\max\|\mathcal{L}\rho_0\| < 3.09\times10^{-14}$.

A useful technique to visualize the stationary state, and distinguish different regimes, is the Wigner quasiprobability function [10]. Nevertheless, a simpler phase space representation is given by the Husimi function, whose computation is more straightforward than the Wigner function and reproduces the same effect. The Husimi function $Q_\rho(\alpha) = \langle\alpha|\,\rho\,|\alpha\rangle$ is defined in terms of the harmonic oscillator (Heisenberg-Weyl) coherent states $|\alpha\rangle = e^{-|\alpha|^2/2}\sum_{n=0}^{N}\frac{\alpha^n}{\sqrt{n!}}|n\rangle$ in the truncated Fock basis. We represent the real part of the Husimi function in Figure 2, separating between electronic diagonal elements $\rho_0^{(+)} = \langle 1|\,\rho_0\,|1\rangle$ (top row) and $\rho_0^{(-)} = \langle 0|\,\rho_0\,|0\rangle$ (bottom row), where $|1\rangle\langle 1| = c^\dagger c$ and $|0\rangle\langle 0| = cc^\dagger$. The columns in the figure panel depict the tunneling, crossover and shuttle regimes from left to right, increasing the value of χ. In the tunneling regime, the stationary solution has the form of the ground state centered in the origin of phase space, while in the shuttle regime it has the toroidal shape characteristic of the time-averaged distribution of a coherent state, which oscillates around the center of phase space.

Quantum transport is commonly described within the framework of a Markovian ME, which can be written in Lindblad form as

$$\frac{d}{dt}\rho = \mathcal{L}\rho, \quad \mathcal{L} = \mathcal{L}_0 + \mathcal{L}_1. \quad (5)$$

Here, the Lindbladian $\mathcal{L}$ is decomposed into two contributions. The term $\mathcal{L}_0$ describes the no-jump evolution, while $\mathcal{L}_1 = \sum_{k=1}^{M}\mathcal{J}_k$ collects M different types of jump

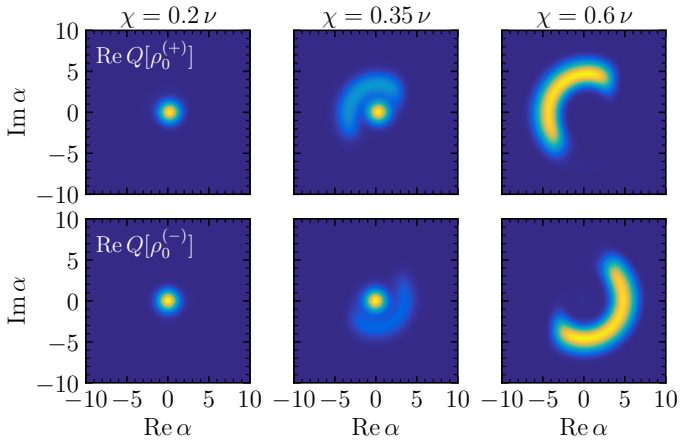


FIG. 2: Husimi function $Q[\rho_0^{(\pm)}] = Q_{\rho_0^{(\pm)}}(\alpha)$ of the stationary solution in the electronic diagonal elements subspaces $\rho_0^{(+)} = \langle 1|\,\rho_0\,|1\rangle$ (top row) and $\rho_0^{(-)} = \langle 0|\,\rho_0\,|0\rangle$ (bottom row), for three values of the electric field $\chi = 0.2\nu, 0.35\nu, 0.6\nu$ in the tunneling, crossover and shuttle regimes respectively (left to right columns). The axis represent the real and imaginary part of the phase space parameter α. The parameters used are $\Gamma = 0.01\nu$, $\kappa = 0.05\nu$, $\lambda = 2x_0$ and an oscillator basis of size $N = 50$.

(tunneling) processes. In our case of interest (3), we will single out the electron tunneling into the dot

$$\mathcal{L}_1\rho = \mathcal{J}\rho = \Gamma c^\dagger e^{-x_0(a^\dagger+a)/\lambda}\,\rho\, c e^{-x_0(a^\dagger+a)/\lambda}. \quad (6)$$

Equivalent results can be obtained by considering the tunneling from the island to the drain.

A formal solution of the master equation can be obtained by expanding the dynamics around the evolution generated by $\mathcal{L}_0$, leading to an expression in terms of conditioned density operators [20, 46, 48, 50, 51]. They describe the non-unitary time-evolution of an initial density operator, which is interrupted by different types and amounts of quantum jumps. In the case of only two jumps, the conditioned density operator has a normalization factor called the waiting time distribution (WTD). Restricted to the case of two jumps of the same type $\mathcal{J}$ (6), occurring at times $t_1 = 0$ and $t_2 = \tau$, the WTD is simply

$$w(\tau) = \frac{\mathrm{tr}(\mathcal{J}e^{\mathcal{L}_0\tau}\mathcal{J}\rho_0)}{\mathrm{tr}(\mathcal{J}\rho_0)}, \quad (7)$$

where we select the stationary solution $\mathcal{L}\rho_0 = 0$ as the initial density operator. For more details on the explicit calculation of the WTD in the vectorized space, see Appendix B, and particularly Eq.(B7).

According to definition (7), the WTD quantifies the conditional probability distribution of two tunneling events separated by a time interval τ. This definition is restricted to the long-time limit, where the system reaches a stationary state [25] and the time translational invariance is present [45]. From the WTD, the mean waiting time can be defined as

$$\langle\tau\rangle = \int_0^\infty \tau\, w(\tau) d\tau, \quad (8)$$

and its standard deviation $\sigma_\tau = \sqrt{\langle(\tau - \langle\tau\rangle)^2\rangle}$. Let us introduce the Fano factor $I = \sigma_\tau^2/\langle\tau\rangle^2$ which provides a measure of the relative fluctuations in the waiting times and therefore of the signal-to-noise ratio [25]. The Fano factor is also presented in the literature as a quotient between the second (zero-frequency noise) and the first (mean value) cumulants of the current [19, 52]. This approach is based on full counting statistics, the stochastic theory of charge transfer through mesoscopic systems [53, 54].

We plot the waiting time distribution (7) in Figure 3, as a function of the coupling χ (in ν units) and the waiting times (in ν^{-1} units). The parameters used are common along the figures, which are $\Gamma = 0.01\nu$, $\kappa = 0.05\nu$, $\lambda = 2x_0$ and an oscillator basis of size $N = 50$. The WTD has been calculated in a 1000 element time window of $\tau \in [0, 300\nu^{-1}]$, with logarithmic scale to increase the point density for low waiting times. This scaling becomes crucial for a non-adaptive integration routine, as the mean waiting time quickly decreases when reaching the shuttle regime, as we will show in Figure 4. On the left part of Figure 3, we see oscillatory patterns for the different vertical sections of fixed χ. That is, the WTD consists of two distinct contributions: a long-time envelope, whose mean waiting time decreases with increasing χ and whose shape is characteristic of single-electron tunneling [25, 55, 56]; and a superimposed oscillatory component associated with the mechanical motion of the shuttle. When increasing χ, these oscillations vanish and the feature at the period of the oscillator $2\pi/\nu$ (identified with a dashed line) increases, reaching its maximum on the right side of the figure for the shuttle regime.

In addition, we display the mean waiting time (8) in Figure 4, derived from the waiting time distribution of the electron shuttle (7). The parameters used are the same as in Figure 4, and so is the waiting time window. The mean waiting time stagnates at $2\pi/\nu$ in the shuttle regime (high χ), while it increases monotonically when moving to the tunneling regime (low χ). In the same Figure 4, we plot the standard deviation and the Fano factor for the same parameters. Both magnitudes display an inflection point and maximum, respectively, around $\chi = 0.34\nu$, characterizing the crossover region previously depicted in Figure 2. This is in agreement with the semiclassical version of the model [57], where the Fano factor has a singularity (limit cycle) in the crossover between underdamped tunneling and shuttle regimes [25, 44].

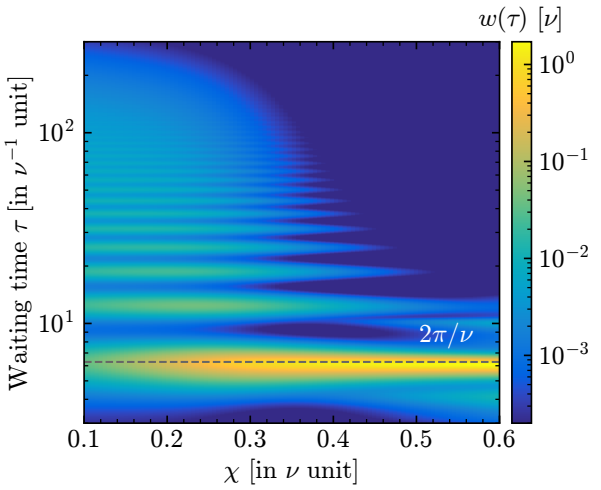


FIG. 3: Heatmap of the waiting time distribution $w(\tau)$ as a function of the coupling χ and the waiting time τ. The logarithmic color scale represents $w(\tau)$ in units of ν. The WTD has been calculated in a 1000 elements time window of $\tau \in [0, 300\nu^{-1}]$, in logarithmic scale to increase the point density for low waiting times. The horizontal dashed line identifies the period of the oscillator in the shuttle regime, $2\pi/\nu$. The parameters used are $\Gamma = 0.01\nu$, $\kappa = 0.05\nu$, $\lambda = 2x_0$ and an oscillator basis of size $N = 50$.

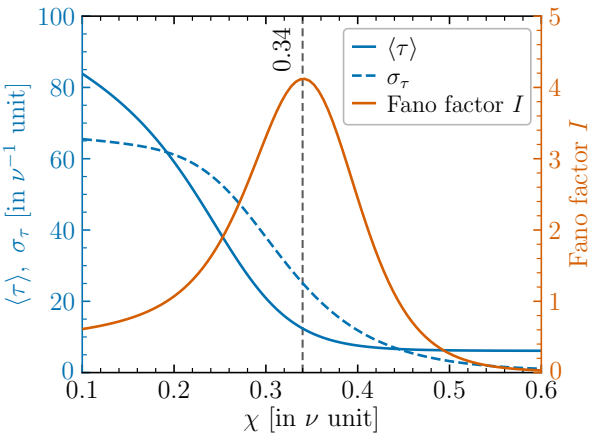


FIG. 4: Mean waiting time (solid blue) and standard deviation (dashed) in ν^{-1} units at the left axis, and Fano factor (orange) at the right axis. Magnitudes are derived from the waiting time distribution of the electron shuttle (7). The parameters used are $\Gamma = 0.01\nu$, $\kappa = 0.05\nu$, $\lambda = 2x_0$ and an oscillator basis of size $N = 50$. The WTD has been calculated in a 1000 elements time window of $\tau \in [0, 300\nu^{-1}]$.

B. Classical and quantum Fisher information

We choose the coupling strength χ, which is proportional to the electric field, as the parameter to be estimated. Since the electric field cannot be measured directly, information about χ must be inferred from measurements performed on n identical realizations of the system in its stationary state, described by the steady-state density matrix ρ_0 of the Lindbladian. In particular, we consider measurements of the waiting time τ between consecutive tunneling events. From the resulting waiting-time distribution (WTD), $w(\tau|\chi)$ (7), which plays the role of the likelihood function, one can construct an estimator for χ and thereby infer the value of the electric field.

The achievable precision of the measurement is bounded by the Cramér-Rao bound

$$\Delta\chi^2 \geq \frac{1}{F(\chi)}\,, \tag{9}$$

where $F(\chi) = nF_1(\chi)$ is the classical Fisher information (CFI), defined as the Fisher information of one measurement $F_1(\chi)$ multiplied by the number n of independent measurements on identical copies of the probe state. The function $F_1(\chi)$ is defined using the waiting time distribution as a likelihood function [58], that is

$$F_1(\chi) = \int_0^\infty \left(\frac{\partial}{\partial\chi}\log w(\tau|\chi)\right)^2 w(\tau|\chi)\,d\tau, \tag{10}$$

as usually for unbiased estimators and independent measures. In practice, the upper bound of the integral is truncated to a finite value $t_{\max}$ when the WTD asymptotically vanishes. For continuously measured quantum systems, the number of measurements $n = T/\langle\tau\rangle$ approaches the quotient of the total measured time T and the measurements mean time $\langle\tau\rangle$, which is equivalent to the mean time between the tunneling events or the mean waiting time (8) [59, 60]. The CFI rate $F(\chi)/T = F_1(\chi)/\langle\tau\rangle$ is independent of the measurement time T and is shown in the bottom panel of Figure 5. Using the same parameters as in Figure 4, we see how this quantity reaches its maximum around $\chi = 0.32\nu$, detecting the crossover region close to the maximum of the Fano factor. At the top of the same figure we represent the CFI for a single measurement (10), whose maximum is slightly shifted to the left compared to the bottom panel.

There is an upper bound for the CFI that results from maximization over all possible measurements [35]: the quantum Fisher information (QFI) [61–64]. For a continuous-measurement metrology paradigm and a sufficiently long measurement time T, the QFI for the estimation of the parameter χ is given asymptotically by [59, 60],

$$F_Q[\rho_0] = -4T\,\mathrm{tr}\left[(\tfrac{1}{\hbar}\partial_\chi H)\mathcal{L}^+(\{\rho_0, \tfrac{1}{\hbar}\partial_\chi H\})\right]. \tag{11}$$

Note that this expression is only valid for a system where the estimation parameter χ is encoded in the Hamiltonian H, not in the jump superoperators. This is precisely our case as shown in eq.(2) and eq.(3). The derivative terms have the simple form $\frac{1}{\hbar}\partial_\chi H = c^\dagger c(a^\dagger + a)$

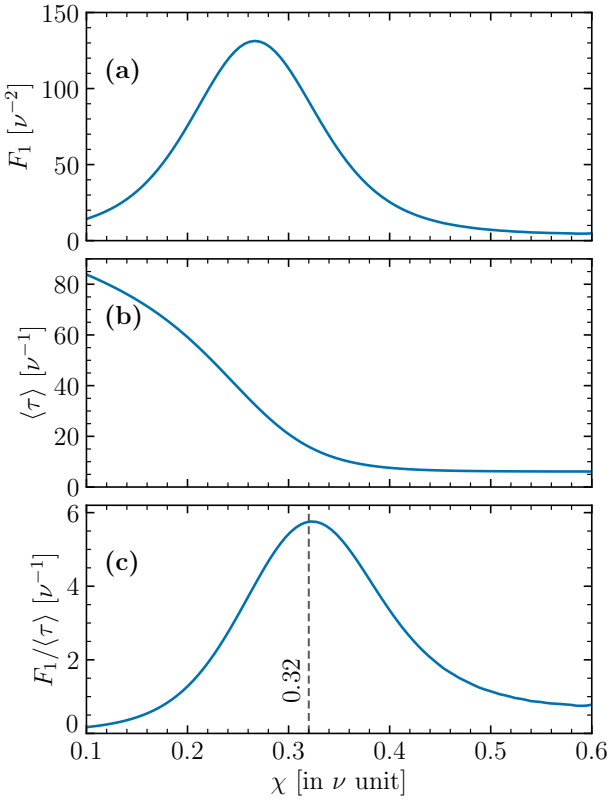


FIG. 5: Classical Fisher Information of a single measurement (10) **(a)**, mean waiting time (8) **(b)**, and CFI of multiple measurements divided by the measurement time $F(\chi)/T = F_1/\langle\tau\rangle$ **(c)**. Magnitudes are in time units (ν^{-1}, except from **(a)** in ν^{-2}), and are derived from the waiting time distribution of the electron shuttle (7). The parameters used are $\Gamma = 0.01\nu$, $\kappa = 0.05\nu$, $\lambda = 2x_0$ and an oscillator basis of size $N = 50$. The WTD has been calculated in a 1000 elements time window of $\tau \in [0, 300\ \nu^{-1}]$.

(2). The symbol $\mathcal{L}^+$ represents the Drazin pseudoinverse [65], whose calculation requires diagonalizing the Lindbladian. However, we consider another method that is less computationally intensive and consists of solving a linear equation system, as we did with the WTD [see Appendix B, and specially eqs.(B7),(B8),(B9), for a detailed explanation].

In the blue line of Figure 6, we represent the QFI rate (QFI divided by T), so it is independent of the measurement time. As the Drazin pseudoinverse has ν^{-1} units and $\frac{1}{\hbar}\partial_\chi H$ is dimensionless, the QFI rate has ν^{-1} units, as the CFI rate in Figure 5. Although the QFI presents a peak for a slightly higher value $\chi = 0.37$ than the CFI plot, the crossover regime is detected in the same region of the coupling parameter. To compare QFI and CFI, we plot in the orange line the quotient between both $F_Q[\rho_0]/F = \frac{F_Q[\rho_0]/T}{F_1/\langle\tau\rangle}$, which is equivalent to dividing the blue line in Figure 6 by the bottom panel of Figure 5. As the QFI is an upper bound for the CFI [61, 66], the orange line in Figure 6 stays above 1 for all χ. The quotient achieves maximum values around the crossover, when the semiclassical version of the model cannot reproduce the effect of its quantum counterpart.

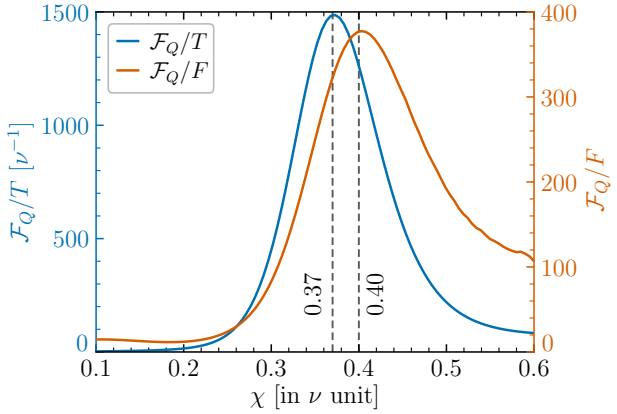


FIG. 6: Quantum Fisher information for a continuous measurement (11) divided by the measurement time T (blue), and QFI divided by the CFI of Figure 5 bottom panel (orange), both as function of the coupling χ. The parameters used are $\Gamma = 0.01\ \nu$, $\kappa = 0.05\ \nu$, $\lambda = 2x_0$ and an oscillator basis of size $N = 50$.

C. Tunneling rate dependence of waiting time sensitivity

In the preceding results, $\Gamma = 0.01\,\nu$ was considered throughout. It is pertinent to inquire whether the sensing ability is an exclusive characteristic of that specific regime or whether it persists when the system is transitioned into qualitatively distinct dynamical regions. Specifically, altering Γ changes the tunneling timescale relative to the mechanical period, thus allowing an investigation into how the tunneling dynamics influences the encoding of the unknown parameter χ in the observed waiting time statistics.

To address this question, we compute the WTD $w(\tau|\chi,\Gamma)$ for the two limiting values $\chi = 0.01\,\nu$ and $\chi = 0.6\,\nu$, and present the results in Fig. 7. The bottom panel **(b)** illustrates the WTD in the high-Γ, fast-tunneling regime, while the top panel **(a)** presents the distributions in the slow-tunneling limit. These curves provide a clear view in the time-domain of how the stochastic detection record responds to variations in χ. The position of the dominant WTD peak indicates the most probable waiting time interval between consecutive detected events. As χ increases from $0.01\,\nu$ to $0.6\,\nu$, the distribution becomes more strongly localized around the mechanical period. Consequently, an increase in χ leads to a more regular electron-emission process, synchronized with the oscillations of the island. This shift is significant for parameter sensing, as χ is inferred not only from the total number of events but also from the redistri-

bution of the probability density along the waiting time axis. The contrast between the top and bottom panels in Fig. 7 demonstrates that this redistribution is highly dependent on the tunneling regime.

This dependence on the tunneling regime is most pronounced at low Γ. In this limit, increasing χ drives the WTD from a broad distribution similar to SET, with a long-time envelope governed by the tunneling timescale $1/\Gamma$, to a sharply localized peak centered around the mechanical period $2\pi/\nu$. The corresponding probability redistribution spans a wide range of waiting times, which implies that changes in χ leave a clear signature in the detection record. As Γ increases and becomes comparable to ν, the influence of mechanical dynamics on emission statistics is progressively reduced. Although the limiting distributions remain distinct, variations in χ produce a less dramatic rearrangement of the probability density, suggesting a weaker dependence of the waiting time statistics on the parameter being estimated. These observations suggest that the amount of information carried by the waiting times should depend strongly on the interplay between the tunneling and mechanical timescales. This motivates a systematic analysis of the Fisher information in the (χ, Γ) parameter space.

A more complete picture is provided by the CFI-rate map shown in Fig. 8. For each value of Γ, the maximum value of the CFI rate identifies the value of χ at which the waiting time statistics are most sensitive. These maxima form a ridge in the (χ, Γ) plane whose position varies non-monotonically with the tunneling rate. For weak tunneling, increasing Γ shifts the maximum CFI toward smaller values of χ. However, beyond a crossover region, the trend reverses and the maximum moves toward larger χ as Γ increases further. Thus, the tunneling rate not only controls the overall magnitude of the achievable sensitivity, but also determines the value of χ at which that sensitivity is optimized.

Fixed-Γ sections of this map are shown in Appendix C, Fig. 9, making explicit both the displacement and the suppression of the maximum sensitivity as Γ increases. Sensitivity arises from a balance between the rate at which tunneling events are accumulated, the dependence of the shape of the WTD on χ, and the suppression of oscillator-mediated features at large Γ. Although increasing Γ reduces characteristic waiting times, sufficiently fast tunneling weakens the mechanical features that carry information about χ. This explains why the optimal sensing performance is obtained in the slow-tunneling regime rather than at the largest values of Γ.

Interestingly, the trajectory of the CFI ridge is qualitatively consistent with the boundary separating the small- and large-Fano-factor regimes identified in our previous study of the classical shuttle [25]. The crossover that organizes the current fluctuations, therefore, also appears to be reflected in the parameter dependence of the waiting time statistics. This correspondence suggests that the competition between mechanical motion and tunneling dynamics determines both the transport noise properties and the parameter region in which waiting time measurements provide the highest sensitivity.

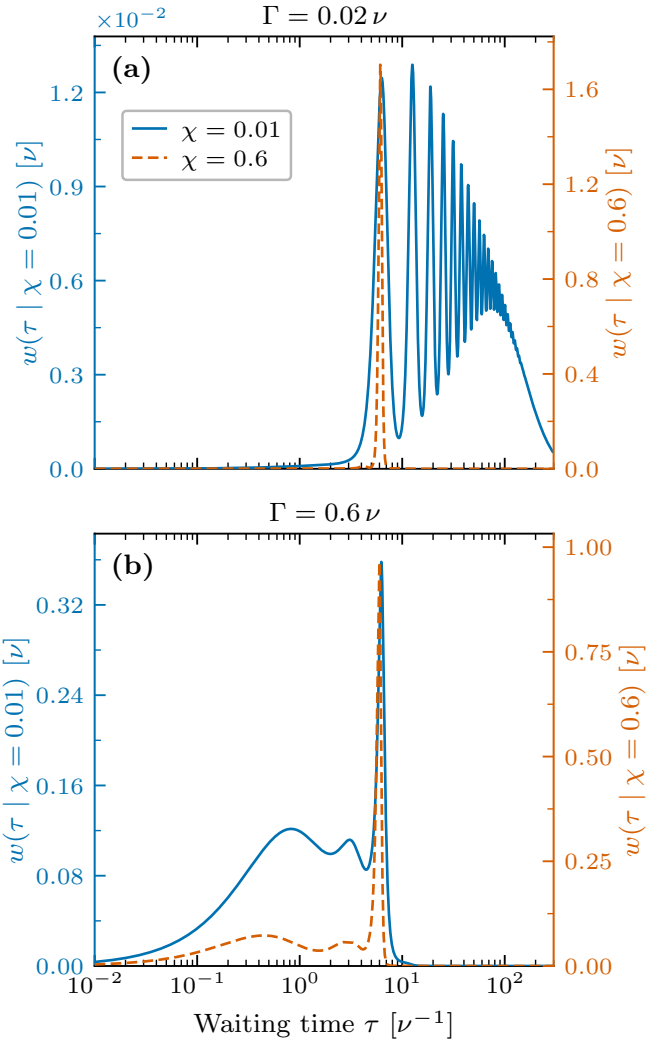


FIG. 7: waiting time distributions $w(\tau|\chi, \Gamma)$ for $\chi = 0.01\,\nu$ (solid blue, left axis) and $\chi = 0.6\,\nu$ (dashed orange, right axis). Panels **(a)** and **(b)** correspond to $\Gamma = 0.02\,\nu$ and $\Gamma = 0.6\,\nu$, respectively. The logarithmic time axis reveals the distinct short- and long-time structures of the distributions. **(a)** For low Γ, the distribution at $\chi = 0.01\,\nu$ exhibits a sequence of oscillatory peaks at multiples $\tau_n = 2\pi n/\nu$ extending toward long waiting times (SET), whereas the distribution at $\chi = 0.6\,\nu$ is concentrated around a narrow peak at $\tau = 2\pi/\nu$ (shuttle). **(b)** In the fast-tunneling regime, the characteristic waiting time scale of the low-χ distribution is shortened and its mechanical harmonics are attenuated. The remaining parameters are $\kappa = 0.05\,\nu$, $\lambda = 2x_0$, and $N = 50$. The WTDs were evaluated on a 2000-point time grid over $\tau \in [0, 300\,\nu^{-1}]$.

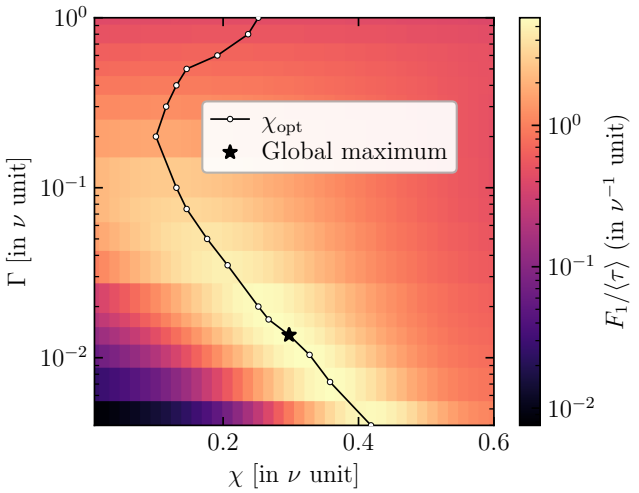


FIG. 8: Classical Fisher information (CFI) rate $F_1(\chi,\Gamma)/\langle\tau\rangle$ across the (χ,Γ) parameter space. Both the vertical Γ axis and the CFI-rate color scale are logarithmic. For each sampled value of Γ, the white circles connected by the black line identify $\chi_{\rm opt}(\Gamma)$, the value of χ that maximizes the CFI rate. The black star marks the global maximum over the sampled grid, located at approximately $\chi \simeq 0.30\,\nu$ and $\Gamma = 0.0136\,\nu$. The remaining parameters are $\kappa = 0.05\,\nu$, $\lambda = 2x_0$, and $N = 50$. The WTDs used in these calculations were evaluated on a 2000-point time grid over $\tau \in [0, 300\,\nu^{-1}]$.

D. Comparison to trapped ions

Estimating weak electric fields is a central task in quantum sensing, and a variety of quantum platforms have been proposed and experimentally realized for this purpose. In this work, we focus on an electron shuttle, in which the electric field couples directly to the mechanical motion of a charged nanostructure. To assess the performance of this approach, it is useful to compare it with alternative sensing architectures.

Among the most successful quantum-sensing platforms are trapped ions. Trapped-ion experiments are often formulated as force- or displacement-sensing protocols, although the associated Fisher information can be translated into electric-field Fisher information. In the protocol of Wolf *et al.* [36], the ion is displaced by an electric field oscillating resonantly at the trap frequency. This provides a common metrological parameterization, although the shuttle responds to a bias-induced field whereas the trapped-ion benchmark concerns the amplitude of a resonant AC field.

Related theoretical studies have investigated quantum-enhanced displacement estimation and force sensing in trapped ions [67, 68]. Once the field-to-displacement conversion and the observation time are specified, the Fisher information of both platforms can be expressed in terms of the relevant electric-field amplitude. We therefore compare the time-normalized electric-field Fisher information of both platforms by translating the Fisher information associated with the measured displacement into the Fisher information for electric-field estimation. Beyond benchmarking the present shuttle implementation, this comparison allows us to identify the physical parameters that should be optimized to approach the sensitivity achieved with trapped ions.

In the shuttle, the parameter to be estimated is χ, which is proportional to the electric field E according to $\hbar\chi = ex_0E$. Consequently, the Fisher information associated with the electric field is

$$F(E) = \left(\frac{ex_0}{\hbar}\right)^2 F(\chi). \tag{12}$$

In trapped-ion force sensing experiments the displacement is typically parameterized by the total coherent displacement amplitude α. Because the accumulated displacement scales linearly with the interrogation time t_i, the corresponding single shot Fisher information for trapped ions F_i can be written as

$$F_i(E) = n\left(\frac{ex_{0,i}t_i}{\hbar}\right)^2 F_i(\alpha), \tag{13}$$

with $x_{0,i} = \sqrt{\hbar/(2m_i\nu_i)}$ the zero point motion of an ion of mass m_i in a trap of frequency ν_i and $n = T/t_i$. Therefore, the ratio of the two sensitivities becomes

$$\frac{F(E)}{F_i(E)} = \frac{m_i\nu_i}{m\nu}\frac{F_1(\chi)}{\langle\tau\rangle t_i F_i(\alpha)}. \tag{14}$$

Equation (14) shows that, for current shuttle realizations, the primary limitation is the mechanical oscillator's large effective mass relative to that of a single trapped ion. However, the shuttle produces a continuous sequence of tunneling events, allowing information to be accumulated from successive waiting time measurements. The two main routes to improve electric-field sensitivity are therefore to reduce $m\nu$ and to increase the Fisher information rate extracted from the transport record by decreasing $\langle\tau\rangle$.

Therefore, achieving the trapped-ion benchmark considered here requires either higher Fisher information for the shuttle, a lighter oscillator, or both. Fisher information can be increased by operating around the crossover, where it peaks, and by using measurements that recover more of quantum Fisher information than waiting time measurements alone. The mechanical limitation can be mitigated by using atomic-scale quantum dots or other nanomechanical devices with masses below those of current shuttle realizations. Such systems could retain the enhanced response around the crossover while increasing the zero-point motion. The comparison therefore identifies three routes to improve shuttle sensing: reducing $m\nu$, operating around the crossover, and extracting more information from the transport record.

IV. CONCLUSIONS

We have investigated electron waiting times in a noisy quantum shuttle and compared them with the total parameter sensitivity in the stationary island-oscillator state. The Husimi distributions demonstrate the transition from a localized tunneling regime to a shuttling regime. The waiting time distributions reveal significant changes in transport statistics as the electromechanical coupling increases. This reorganization is also reflected in the first two moments of the waiting time distribution. The mean waiting time decreases as mechanically assisted transport becomes established, whereas the Fano factor shows a pronounced enhancement in the crossover region before fluctuations are suppressed in the more regular shuttling regime. The crossover is therefore the noisiest operating region in relative terms, even though it is also the region where the dynamics respond most strongly to changes in the electromechanical coupling.

Treating the coupling strength, and hence the applied electric field, as an unknown parameter, we used classical and quantum Fisher information to quantify the response. Under the same resource normalization, the waiting time Fisher information remains below the quantum Fisher information across all regimes studied. Hence, monitoring the time intervals between tunneling events does not fully recover information about the joint electronic and mechanical degrees of freedom. The comparison links noise to metrological sensitivity, revealing increased fluctuations that signal transport dynamics sensitive to electromechanical coupling. The Fano factor and Fisher information peak in the same region. However, since noise and information measurements are not identical, they may peak at different parameters.

These findings establish that waiting time measurements provide a transparent, relevant sensing protocol, while quantum Fisher information offers a comprehensive benchmark for identifying the best operating point or comparing measurement strategies. For evaluating the device's sensing potential, determining optimal conditions, or comparing detection schemes, quantum Fisher information is the best figure of merit. Future work could measure them near the quantum limit, compare them at the level of monitored trajectories, and assess robustness to temperature, tunneling asymmetry, detector inefficiency, and non-Markovian environments.

V. DECLARATIONS

A. Ethics Approval

Not applicable.

B. Funding

All authors acknowledge support from grant CNS2023-144994 funded by MICIU/AEI/10.13039/201100011033 and "ERDF/EU" and from European Union project C-QuENS (Grant No. 101135359). A.L.G., E.H. and J.C. acknowledge support from the Gobierno de la Región de Murcia through the Programa Regional de Fomento de la Investigación Científica y Técnica (convocatoria de ayudas a Grupos de Excelencia de la Fundación Séneca 2026–2029, Grant No. 23026/GERM/25). A.M. additionally acknowledges support of the Spanish Ministry of Science through the project PID2022-138144NB-I00.

Appendix A: Approximations in the master equation

In the following, we present a series of approximations necessary to obtain the simplified ME in (3). Firstly, it is enlightening to show the full expression of the total Hamiltonian (1) according to the references [44, 45],

$$\begin{aligned} H_{\mathrm{T}} = \; & \hbar\omega_{\mathrm{I}} c^\dagger c + U_c (c^\dagger c)^2 + \hbar\nu a^\dagger a - \hbar\chi c^\dagger c (a^\dagger + a) && (H_{\mathrm{S}}) \\ & + \textstyle\sum_k (\hbar\omega_{sk} c_k^\dagger c_k + \hbar\omega_{dk} d_k^\dagger d_k) && (H_{\mathrm{L}}) \\ & + \textstyle\sum_k (T_{sk} e^{-\hat{x}/\lambda} c_k c^\dagger + \mathrm{H.c.}) && (H_{\mathrm{tun}}) \\ & + \textstyle\sum_k (T_{dk} e^{\hat{x}/\lambda} d_k c^\dagger + \mathrm{H.c.}) \\ & + \textstyle\sum_p \left[\hbar\omega_p b_p^\dagger b_p + g(a^\dagger b_p + a b_p^\dagger) \right] && (H_{\mathrm{B}}) \end{aligned} \tag{A1}$$

Comparing with eq.(2), in the system Hamiltonian H_{S}, the strong Coulomb blockade regime ensures that no more than one electron occupies the island at any time, so that the number operator fulfills $(c^\dagger c)^2 = c^\dagger c$ and we can define a single effective energy level $\varepsilon_I = \hbar\omega_{\mathrm{I}} + U_c$. The leads Hamiltonian H_{L} describes the electrostatic energy of an ensemble of non-interacting electrons c_k and d_k, described by the Fermi distribution. The tunneling Hamiltonian H_{tun} couples the island, the leads, and the oscillator via the exponential of the position operator $\hat{x} = \sqrt{\frac{\hbar}{2m\nu}}(a + a^\dagger)$. The bath Hamiltonian H_{B} couples the oscillator to a dissipative Ohmic heat bath (bosonic b_p) in the rotating wave approximation.

The interaction of the system H_{S} (2) with the bosonic heat bath H_{B} has decoherence effects, so that the initial quantum state, in absence of driving force, evolves to a thermal stationary distribution (diagonal density matrix) at long time. This relaxation towards canonical equilibrium, the translational invariance that shows the damping term, and the positivity of the density matrix are incompatible with a Markovian damping kernel [10]. Therefore, we weaken the positivity as in [69]. Nevertheless, we checked numerically that the positivity is only broken for large values of the damping κ out of the

shuttle regime, in accordance with [10, 49]. As an additional approximation, we set the damping rate κ constant, fixing the density of states of the phonon bath and the oscillator-bath coupling [49].

In contrast to the weak coupling (Born approximation) with the thermal bath, the tunneling coupling with the leads is comparable to the oscillator frequency. Hence, in the shuttle regime, the time scale of the electrical dynamics is comparable with the period of the mechanical oscillations in the system. This is why we have considered an arbitrary coupling to the leads approach [70]. Firstly, the island-leads coupling in the ME (3) is computed with the strong Coulomb blockade. This means that once the dot is charged with an electron of specific spin, only that species can tunnel out. This approximation is equivalent to renormalize the injection rate and consider spin-less non-interacting particles in the island [49, 71].

To obtain a Markov master equation for the island-oscillator system, we trace out the degrees of freedom in the leads and use the Born-Markov approximation [48, 72]. That is, we assume the vibrational frequency of the oscillator is slow compared to bath relaxation time scales. The derived ME is [44, 45, 49]

$$\begin{aligned}\frac{d}{dt}\rho = &-i\nu\left[a^\dagger a,\rho\right]+i\chi\left[c^\dagger c(a^\dagger+a),\rho\right]\\ &+\Gamma_L f(\varepsilon_{\rm I}-\mu_L)\,\mathcal{D}\left[c^\dagger e^{-x_0(a^\dagger+a)/\lambda}\right]\rho\\ &+\Gamma_L(1-f(\varepsilon_{\rm I}-\mu_L))\,\mathcal{D}\left[c\,e^{-x_0(a^\dagger+a)/\lambda}\right]\rho\\ &+\Gamma_R f(\varepsilon_{\rm I}-\mu_L)\,\mathcal{D}\left[c^\dagger e^{x_0(a^\dagger+a)/\lambda}\right]\rho\\ &+\Gamma_R(1-f(\varepsilon_{\rm I}-\mu_L))\,\mathcal{D}\left[c\,e^{x_0(a^\dagger+a)/\lambda}\right]\rho\\ &+\kappa(\bar{n}_p+1)\,\mathcal{D}\left[a\right]\rho+\kappa\bar{n}_p\,\mathcal{D}\left[a^\dagger\right]\rho\,. \end{aligned}\tag{A2}$$

We consider leads temperatures much smaller than their Fermi energy, so we can approximate their Fermi distributions $f(\varepsilon_{\rm I}-\mu_{L,R})$ by step functions. The chemical potential of the left (right) lead is assumed much higher (lower) than the dot energy level $\mu_L \gg \varepsilon_{\rm I} \gg \mu_R$. We also consider the high bias approximation, that is the tunneling amplitude and density of states of the leads are constant, making constant the injection and ejection rates $\Gamma=\Gamma_L=\Gamma_R$ (we additionally set both equal) [72]. We have also disregarded cotunneling and higher order scattering events. The local thermodynamic equilibrium in the leads makes that any correlation, between the electrons in the leads and in the island, rapidly decays to zero, as a result of the tunneling interaction and on time scales relevant for the system dynamics [72]. The Bose-Einstein distribution $\bar{n}_p$ of the bath, in thermal equilibrium, is also approximated to 0 [19]. All together leads to the reduced ME (3).

The last approximation deriving the ME driving terms $\mathcal{D}\left[c^{(\dagger)}e^{\pm(a^\dagger+a)/\lambda}\right]\rho$ (island-oscillator-leads coupling), is to assume that the position of the system energy levels should be contained in the transport window open between the chemical potentials of the leads. To be precise, only a finite number of mechanical excitations are involved in the dynamics of the system, which means a truncation of the oscillator basis. Even in the presence of the bath, this assumption is numerically accomplished in the cases of study, being the violation of this condition incongruent with the validity of the ME.

Appendix B: Vectorization of the island-oscillator system

The density matrices solution of the master equation (3) belong to the tensor product Hilbert space of the island-oscillator $\mathcal{H}_I\otimes\mathcal{H}_O$. The oscillator space is truncated to dimension N for numerical calculations, hence the density matrix has a size $2N\times 2N$. In order to solve the ME, we perform a vectorization to express the matrix multiplication as a linear transformation. That is, $A\in\mathcal{M}_{2N,2N}(\mathbb{C})$ matrices are transformed into $\mathrm{vec}(A)\in\mathcal{M}_{4N^2,1}(\mathbb{C})$ column vectors, and the following expressions are used

$$\mathrm{vec}(ABC)=(C^T\otimes A)\mathrm{vec}(B),\tag{B1}$$

$$\mathrm{vec}(AB)=(I_{2N}\otimes A)\mathrm{vec}(B)=(B^T\otimes I_{2N})\mathrm{vec}(A),\tag{B2}$$

$$\mathrm{tr}(A^\dagger B)=\mathrm{vec}(A)^\dagger\mathrm{vec}(B),\tag{B3}$$

for all $A\in\mathcal{M}_{2N,2N}(\mathbb{C})$, where $I_{2N}=I_2\otimes I_N$ is the identity matrix of the island-oscillator space. The commutator and dissipator terms in the ME (3) are transformed into

$$\mathrm{vec}([A,\rho])=(I_{2N}\otimes A-A^T\otimes I_{2N})\mathrm{vec}(\rho),\tag{B4}$$

$$\begin{aligned}\mathrm{vec}(\mathcal{D}[A]\rho)=&(A^*\otimes A)\mathrm{vec}(\rho)\\ &+\frac{1}{2}(I_{2N}\otimes A+A^T\otimes I_{2N})\mathrm{vec}(\rho).\end{aligned}\tag{B5}$$

The problem of calculating the stationary solution of the ME $\mathcal{L}\rho_0=0$ is reduced to solving a system of linear equations $\mathrm{vec}(\mathcal{L}\rho_0)=L\,\mathrm{vec}(\rho_0)=0$, where L is a $4N^2\times 4N^2$ matrix obtained by applying Eqs.(B4),(B5) to the ME (3). The linear system dimensions increase by one because of the extra normalization condition $\mathrm{tr}(\rho)=\mathrm{vec}(I_{2N})^T\mathrm{vec}(\rho)=1$ as in references [20, 52]. The solution of the system is computed using the MatLab© *mldivide* routine, that combines brute force and LU solver. It is worth mentioning that other works use the Arnoldi scheme (Krylov spaces, singular value decomposition and preconditioning) to reduce the dimensionality and accelerate the computations [10, 19, 49, 73].

The jump operator chosen in Eq.(6) has a vectorized form

$$\begin{aligned}\mathrm{vec}(\mathcal{J}\rho)=&\,\Gamma(c^\dagger e^{-x_0(a^\dagger+a)/\lambda})\otimes(c^\dagger e^{-x_0(a^\dagger+a)/\lambda})\mathrm{vec}(\rho)\\ =&\,J\,\mathrm{vec}(\rho),\end{aligned}\tag{B6}$$

where J is the $4N^2 \times 4N^2$ superoperator form. The waiting time distribution in Eq.(7) is also vectorized as

$$w(\tau) = \frac{\mathrm{vec}(I_{2N})^T J V e^{D\tau} V^{-1} J \mathrm{vec}(\rho_0)}{\mathrm{vec}(I_{2N})^T \mathrm{vec}(\rho_0)}. \tag{B7}$$

The symbols represent V and D represent the eigenvector and eigenvalues matrices derived from the Lindbladian L_0 after the vectorization, that is, $\mathrm{vec}(\mathcal{L}_0\rho) = L_0\mathrm{vec}(\rho)$ (see Eq.(5)). Note that, instead of computing the inverse matrix V^{-1}, it is easier to solve the equation system $VX = J\mathrm{vec}(\rho_0)$. In addition, the WTD is computed for a finite number of points in the τ-domain as $w \xrightarrow{\tau\to\infty} 0$, that is, we truncate up to certain value $\tau = t_{\max}$ coinciding with the upper bound in the CFI integral (10).

The QFI expression (11) can also be vectorized to simplify its calculation. Firstly, we use the eq.(B3), so that the QFI transforms into

$$-4T\,\mathrm{tr}\left[(\tfrac{1}{\hbar}\partial_\chi H)\mathcal{L}^+ B\right] = \mathrm{vec}(\tfrac{1}{\hbar}\partial_\chi H^\dagger)^\dagger\,\mathrm{vec}(\mathcal{L}^+ B)\,, \tag{B8}$$

where we have defined $B = \{\rho_0, \frac{1}{\hbar}\partial_\chi H\}$ to simplify the notation. Instead of diagonalizing the Lindbladian and computing $\mathcal{L}^+$, we define $X = \mathcal{L}^+ B$ and multiply this expression by $\mathcal{L}$ to obtain $\mathcal{L}X = \mathcal{L}\mathcal{L}^+ B$. The product $\mathcal{L}\mathcal{L}^+$ reduces to $\mathbb{1} - \mathrm{vec}(\rho_0)\mathrm{vec}(I_{2N})^T$ when vectorizing, which is the identity on the subspace complementary to that defined by $\mathrm{vec}(\rho_0)\mathrm{vec}(I_{2N})^T$ [59]. Then, we can write the equation system

$$L\,\mathrm{vec}(X) = (\mathbb{1} - \mathrm{vec}(\rho_0)\mathrm{vec}(I_{2N})^T)\mathrm{vec}(B) \tag{B9}$$

where L comes from the vectorization of $\mathrm{vec}(\mathcal{L}\rho) = L\,\mathrm{vec}(\rho)$. Eventually, the solution of the system $\mathrm{vec}(X)$ is equivalent to the term $\mathrm{vec}(\mathcal{L}^+ B)$ by definition, and the QFI can be computed in the vectorized version of eq.(B8).

Appendix C: Fixed tunneling rate sections of the classical Fisher information rate

To complement the two-dimensional map shown in Fig. 8, Fig. 9 presents fixed-Γ cuts of the classical Fisher-information rate. These curves make explicit both the displacement and the suppression of the sensitivity maximum as the tunneling rate increases.

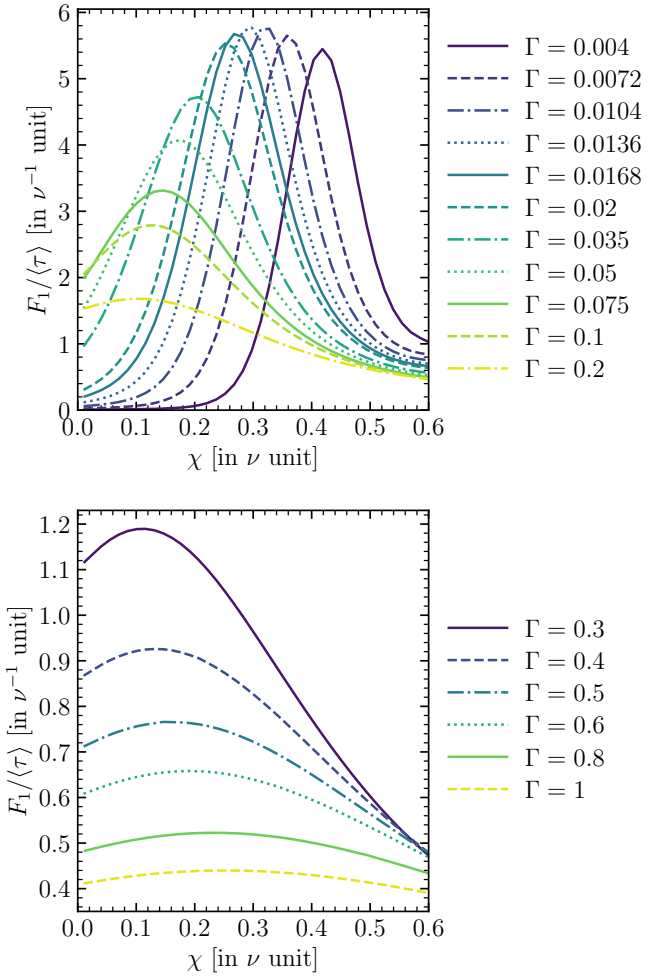


FIG. 9: Classical Fisher information rate, $F_1(\chi,\Gamma)/\langle\tau\rangle$, as a function of χ for selected tunneling rates. The upper panel shows the low- and intermediate-rate region, $0.004\,\nu \le \Gamma \le 0.2\,\nu$, whereas the lower panel shows the high-rate region, $0.3\,\nu \le \Gamma \le 1\,\nu$. These curves correspond to fixed-Γ cuts of the map in Fig. 8 and illustrate both the shift and suppression of the sensitivity maximum as Γ increases. The remaining parameters are $\kappa = 0.05\,\nu$, $\lambda = 2x_0$, and $N = 50$.

REFERENCES

[1] L. Gorelik, A. Isacsson, M. Voinova, B. Kasemo, R. Shekhter, and M. Jonson, Shuttle mechanism for charge transfer in Coulomb blockade nanostructures, Physical Review Letters **80**, 4526 (1998).

[2] D. V. Scheible, A. Erbe, and R. H. Blick, Tunable coupled nanomechanical resonators for single-electron transport, New Journal of Physics **4**, 86 (2002).

[3] M. T. Tuominen, R. V. Krotkov, and M. L. Breuer, Stepwise and hysteretic transport behavior of an electromechanical charge shuttle, Physical Review Letters **83**, 3025 (1999).

[4] H. Park, J. Park, A. K. L. Lim, E. H. Anderson, A. P. Alivisatos, and P. L. McEuen, Nanomechanical oscillations in a single-C60 transistor, Nature **407**, 57 (2000).

[5] A. Armour and A. MacKinnon, Transport via a quantum shuttle, Physical Review B **66**, 035333 (2002).

[6] A. Bachtold, J. Moser, and M. Dykman, Mesoscopic physics of nanomechanical systems, Reviews of Modern Physics **94**, 045005 (2022).

[7] T. Novotnỳ, A. Donarini, and A.-P. Jauho, Quantum shuttle in phase space, Physical Review Letters **90**, 256801 (2003).

[8] D. W. Utami, H.-S. Goan, C. A. Holmes, and G. J. Milburn, Quantum noise in the electromechanical shuttle: Quantum master equation treatment, Physical Review B **74**, 014303 (2006).

[9] L. Y. Gorelik, A. Isacsson, M. V. Voinova, B. Kasemo, R. I. Shekhter, and M. Jonson, Shuttle mechanism for charge transfer in Coulomb blockade nanostructures, Physical Review Letters **80**, 4526 (1998).

[10] T. c. v. Novotný, A. Donarini, and A.-P. Jauho, Quantum shuttle in phase space, Physical Review Letters **90**, 256801 (2003).

[11] D. Fedorets, Quantum description of shuttle instability in a nanoelectromechanical single-electron transistor, Physical Review B **68**, 033106 (2003).

[12] D. Fedorets, L. Y. Gorelik, R. I. Shekhter, and M. Jonson, Quantum shuttle phenomena in a nanoelectromechanical single-electron transistor, Physical Review Letters **92**, 166801 (2004).

[13] A. Armour, M. Blencowe, and Y. Zhang, Classical dynamics of a nanomechanical resonator coupled to a single-electron transistor, Physical Review B **69**, 125313 (2004).

[14] F. Pistolesi, Full counting statistics of a charge shuttle, Physical Review B **69**, 245409 (2004).

[15] Y. M. Blanter and M. Büttiker, Shot noise in mesoscopic conductors, Physics Reports **336**, 1 (2000).

[16] L. S. Levitov, H. Lee, and G. B. Lesovik, Electron counting statistics and coherent states of electric current, Journal of Mathematical Physics **37**, 4845 (1996).

[17] C. Emary, D. Marcos, R. Aguado, and T. Brandes, Frequency-dependent counting statistics in interacting nanoscale conductors, Physical Review B **76**, 161404 (2007).

[18] C. Flindt, T. Novotnỳ, A. Braggio, M. Sassetti, and A.-P. Jauho, Counting statistics of non-Markovian quantum stochastic processes, Physical Review Letters **100**, 150601 (2008).

[19] T. c. v. Novotný, A. Donarini, C. Flindt, and A.-P. Jauho, Shot noise of a quantum shuttle, Physical Review Letters **92**, 248302 (2004).

[20] T. Brandes, Waiting times and noise in single particle transport, Annalen der Physik **520**, 477 (2008).

[21] M. Albert, G. Haack, C. Flindt, and M. Büttiker, Electron waiting times in mesoscopic conductors, Physical Review Letters **108**, 186806 (2012).

[22] K. H. Thomas and C. Flindt, Electron waiting times in non-Markovian quantum transport, Physical Review B **87**, 121405 (2013).

[23] G. Haack, M. Albert, and C. Flindt, Distributions of electron waiting times in quantum-coherent conductors, Physical Review B **90**, 205429 (2014).

[24] P. Stegmann, B. Sothmann, J. König, and C. Flindt, Electron waiting times in a strongly interacting quantum dot: Interaction effects and higher-order tunneling processes, Physical Review Letters **127**, 096803 (2021).

[25] C. W. Wächtler and J. Cerrillo, Electron shuttle as an autonomous single-electron source, Physical Review Applied **18**, 014011 (2022).

[26] H. Zhao, Y. Ding, J. Tang, G. O. Paul, F. O. Awiti, E. O. Ayieta, S. Kelemen, Y. Su, S. Radošević, G. Engelhardt, *et al.*, Non-Markovian waiting-time distribution for electron transport through a vibrating molecular junction, The Journal of Chemical Physics **163** (2025).

[27] V. Giovannetti, S. Lloyd, and L. Maccone, Advances in quantum metrology, Nature Photonics **5**, 222 (2011).

[28] V. Giovannetti, S. Lloyd, and L. Maccone, Quantum metrology, Physical Review Letters **96**, 010401 (2006).

[29] S. Alipour, M. Mehboudi, and A. Rezakhani, Quantum metrology in open systems: dissipative Cramér-Rao bound, Physical Review Letters **112**, 120405 (2014).

[30] S. Gammelmark and K. Mølmer, Fisher information and the quantum Cramér-Rao sensitivity limit of continuous measurements, Physical Review Letters **112**, 170401 (2014).

[31] R. A. Fisher, Theory of statistical estimation, Mathematical Proceedings of the Cambridge Philosophical Society **22**, 700–725 (1925).

[32] M. M. Müller, S. Gherardini, A. Smerzi, and F. Caruso, Fisher information from stochastic quantum measurements, Physical Review A **94**, 042322 (2016).

[33] Y. Ma, M. Pang, L. Chen, and W. Yang, Improving quantum parameter estimation by monitoring quantum trajectories, Physical Review A **99**, 032347 (2019).

[34] C. W. Helstrom, Quantum detection and estimation theory, Journal of statistical physics **1**, 231 (1969).

[35] S. L. Braunstein and C. M. Caves, Statistical distance and the geometry of quantum states, Physical Review Letters **72**, 3439 (1994).

[36] F. Wolf, C. Shi, J. C. Heip, M. Gessner, L. Pezzè, A. Smerzi, M. Schulte, K. Hammerer, and P. O. Schmidt, Motional Fock states for quantum-enhanced amplitude and phase measurements with trapped ions, Nature Communications **10**, 2929 (2019).

[37] P. Zanardi, M. G. Paris, and L. Campos Venuti, Quantum criticality as a resource for quantum estimation, Physical Review A **78**, 042105 (2008).

[38] I. Frérot and T. Roscilde, Quantum critical metrology, Physical Review Letters **121**, 020402 (2018).

[39] L. Garbe, M. Bina, A. Keller, M. G. Paris, and S. Felicetti, Critical quantum metrology with a finite-component quantum phase transition, Physical Review Letters **124**, 120504 (2020).

[40] T. Ilias, D. Yang, S. F. Huelga, and M. B. Plenio, Criticality-enhanced quantum sensing via continuous measurement, PRX Quantum **3**, 010354 (2022).

[41] T. Ilias, D. Yang, S. F. Huelga, and M. B. Plenio, Criticality-enhanced electric field gradient sensor with single trapped ions, npj Quantum Information **10**, 36 (2024).

[42] U. Alushi, W. Górecki, S. Felicetti, and R. Di Candia, Optimality and noise resilience of critical quantum sensing, Physical Review Letters **133**, 040801 (2024).

[43] G. Mihailescu, U. Alushi, R. Di Candia, S. Felicetti, and K. Gietka, Critical quantum sensing: A tutorial on parameter estimation near quantum phase transitions, PRX Quantum **7**, 020201 (2026).

[44] D. W. Utami, H.-S. Goan, C. A. Holmes, and G. J. Milburn, Quantum noise in the electromechanical shuttle: Quantum master equation treatment, Physical Review B **74**, 014303 (2006).

[45] H. Zhao, Y. Ding, J. Tang, G. O. Paul, F. O. Awiti, E. O. Ayieta, S. Kelemen, Y. Su, S. Radošević, G. Engelhardt, and J. Luo, Non-Markovian waiting-time distribution for electron transport through a vibrating molecular junction, The Journal of Chemical Physics **163**, 194102 (2025).

[46] C. Gardiner and P. Zoller, *Quantum noise* (Springer Berlin, 2004).

[47] U. Weiss, *Qauntum dissipative systems* (Series in Modern Condensed Matter Physics Vol. 10, World Scientific Press, 1999).

[48] H.-P. Breuer and F. Petruccione, *The Theory of Open Quantum Systems* (Oxford University Press, 2007).

[49] A. Donarini, *Dynamics of shuttle devices*, Ph.D. thesis, Technical University of Denmark (2004).

[50] E. Etim and C. Basili, On the path integral solutions of the master equation, Physics Letters A **67**, 246 (1978).

[51] H. Carmichael, *An Open Systems Approach to Quantum Optics* (Springer Berlin Heidelberg, 1993).

[52] C. Flindt, T. Novotný, and A.-P. Jauho, Full counting statistics of nano-electromechanical systems, Europhysics Letters **69**, 475 (2004).

[53] D. A. Bagrets and Y. V. Nazarov, Full counting statistics of charge transfer in Coulomb blockade systems, Physical Review B **67**, 085316 (2003).

[54] C. Flindt, *Electrons in Nanostructures coherent manipulation and counting statistics*, Ph.D. thesis, Technical University of Denmark (2007).

[55] A. Donarini and M. Grifoni, *Quantum Transport in Interacting Nanojunctions: A Density Matrix Approach*, Lecture Notes in Physics, Vol. 1024 (Springer International Publishing, Cham, 2024).

[56] S. Datta, *Quantum Transport: Atom to Transistor* (Cambridge University Press, Cambridge, 2005).

[57] A. Isacsson and T. Nord, Low-frequency current noise of the single-electron shuttle, Europhysics Letters **66**, 708 (2004).

[58] R. A. Fisher, On the mathematical foundations of theoretical statistics, Philosophical Transactions of the Royal Society of London, Series A: Containing Papers of a Mathematical or Physical Character **222**, 309 (1922).

[59] G. T. Landi, M. J. Kewming, M. T. Mitchison, and P. P. Potts, Current fluctuations in open quantum systems: Bridging the gap between quantum continuous measurements and full counting statistics, PRX Quantum **5**, 020201 (2024).

[60] S. Gammelmark and K. Mølmer, Fisher information and the quantum Cramér-Rao sensitivity limit of continuous measurements, Physical Review Letters **112**, 170401 (2014).

[61] L. Pezzè, A. Smerzi, M. K. Oberthaler, R. Schmied, and P. Treutlein, Quantum metrology with nonclassical states of atomic ensembles, Reviews of Modern Physics **90**, 035005 (2018).

[62] D. Petz and C. Ghinea, Introduction to quantum Fisher information, *Quantum Probability and Related Topics*, Quantum probability and white noise analysis , 261 (2016).

[63] E. Polino, M. Valeri, N. Spagnolo, and F. Sciarrino, Photonic quantum metrology, AVS Quantum Science **2**, 024703 (2020).

[64] D. Petz, Covariance and Fisher information in quantum mechanics, Journal of Physics A: Mathematical and General **35**, 929 (2002).

[65] M. P. Drazin, Pseudo-inverses in associative rings and semigroups, The American Mathematical Monthly **65**, 506 (1958).

[66] C. Helstrom, Minimum mean-squared error of estimates in quantum statistics, Physics Letters A **25**, 101 (1967).

[67] J. Cerrillo and D. Rodríguez, Motional quantum metrology in a penning trap, EPL (Europhysics Letters) **134**, 38001 (2021).

[68] A. Delakouras, D. Rodríguez, and J. Cerrillo, Production of Fock mixtures in trapped ions for motional metrology, Quantum Science and Technology **9**, 015006 (2024).

[69] D. Kohen, C. C. Marston, and D. J. Tannor, Phase space approach to theories of quantum dissipation, The Journal of Chemical Physics **107**, 5236 (1997).

[70] S. A. Gurvitz and Y. S. Prager, Microscopic derivation of rate equations for quantum transport, Physical Review B **53**, 15932 (1996).

[71] M. R. Wegewijs and Y. V. Nazarov, Resonant tunneling through linear arrays of quantum dots, Physical Review B **60**, 14318 (1999).

[72] D. W. Utami, H.-S. Goan, and G. J. Milburn, Charge transport in a quantum electromechanical system, Physical Review B **70**, 075303 (2004).

[73] C. Flindt, T. c. v. Novotný, and A.-P. Jauho, Current noise in a vibrating quantum dot array, Physical Review B **70**, 205334 (2004).